

1 Energy and force prediction for a nanosecond pulsed dielectric barrier

2 discharge actuator

3 Chin-Cheng Wang^{a)} and Subrata Roy^{b)}

4 *Applied Physics Research Group, Department of Mechanical and Aerospace Engineering,*
 5 *University of Florida, Gainesville, Florida 32611, USA*

6 (Received 12 February 2012; accepted 28 April 2012; published online xx xx xxxx)

7 A three-species physical model is presented for dielectric barrier discharge (DBD) actuator under
 8 atmospheric pressure. The governing equations are solved for temporal and spatial distribution of
 9 electric potential and charge species using the finite element based multiscale ionized gas flow
 10 code. The plasma model is loosely coupled with compressible Navier-Stokes equations through
 11 momentum and energy source terms. Two cases of rf powered and nanosecond pulsed barrier
 12 discharge actuators are simulated. Based on the imparted time average electrohydrodynamic force
 13 and power deposition to the neutral gas, the nanosecond pulsed DBD actuator creates significant
 14 pressure variations within few microseconds. These results are in reasonable agreement with
 15 recently reported experimental shadow images. © 2012 American Institute of Physics.

16 [http://dx.doi.org/10.1063/1.4722202]

17 I. INTRODUCTION

18 Weakly ionized plasmas in dielectric barrier discharge
 19 (DBD) generated using moderate frequency high voltage
 20 power source have been applied to a number of applications
 21 in the past few decades.¹ At the present time, applications
 22 such as sterilization² for healthcare purposes, flow control³
 23 for the aerospace industries, and flame stability⁴ for the com-
 24 bustion engines are potentially very exciting areas. However,
 25 non-equilibrium DBD plasmas find limited application for
 26 high speed flows. This is due to inherent losses associated
 27 with the momentum exchange between the charged and neutral
 28 particles and due to exorbitant power budget. As an alter-
 29 native, high-voltage nanosecond pulsed DBD plasmas⁵ are
 30 becoming quite attractive option for high speed application.

31 In conventional method, non-equilibrium plasmas can
 32 be generated between two electrodes on the dielectric surface
 33 as an alternating current (AC) passes through them with high
 34 sinusoidal voltage. The dielectric is used to stabilize the dis-
 35 charge without arcing. Such a plasma generating device is
 36 called a DBD actuator. The operational conditions of the
 37 DBD actuator are at frequencies of one to tens of kilohertz
 38 and amplitudes of one to tens of kilovolts in a sinusoidal
 39 type wave. Our recent experiments⁶ showed such conven-
 40 tional AC powered DBD actuator consumes tens of watts per
 41 meter under atmospheric pressure. The value of the power
 42 increased exponentially as the input applied voltage
 43 increased linearly from 14 to 30 kV. If we can minimize the
 44 power required to sustain non-equilibrium plasmas, such
 45 plasma generating device will become very useful.

46 There are a few ways to sustain non-equilibrium plas-
 47 mas with low input applied voltage such as microscale
 48 discharges^{7–9} and nanosecond pulsed discharges.^{10–12}
 49 Macheret *et al.*⁵ presented analytical calculations showing

50 that power budget in nanosecond pulsed discharges can
 51 be significantly lower than that in dc discharges. They pre-
 52 dicted an ionization efficiency (i.e., ionization level/power)
 53 improvement of roughly two orders of magnitude. Also, their
 54 modeling showed there is a strong ionization near the cath-
 55 ode sheath due to non-uniform redistribution of electric
 56 potential. Later on, the Princeton University group showed
 57 both numerical and experimental investigations of the DBD
 58 actuators driven by nanosecond pulses.^{10,11} Both computa-
 59 tions and experiments demonstrated the similar vortical
 60 structures induced by the actuator. Also, the results showed
 61 repetitive short pulses do efficiently generate the plasma.
 62

63 Recently, experimental results of nanosecond pulsed
 64 plasma actuator by Starikovskii *et al.*¹² have reported that
 65 nanosecond pulsed voltage is highly efficient to control
 66 boundary layer separation, lift and drag force coefficients, in
 67 addition to acoustic noise reduction in the Mach number
 68 range 0.05–0.85 compared with AC sinusoidal voltage. More
 69 significantly, they concluded that there is a fundamental dif-
 70 ference between nanosecond pulsed discharge and conven-
 71 tional AC driven discharge for the plasma-flow interaction.
 72 In the case of conventional DBD actuator, the main mecha-
 73 nism of impact is the momentum transfer from electric field
 74 to the near surface gas. In contrast, for nanosecond pulsed
 75 DBD actuator, the main mechanism of impact is the energy
 76 transfer to the gas near the surface. Their measurements
 77 showed the mean values of such heating can reach 400 K for
 78 50 ns pulse durations. Such fast heating (less than microsec-
 79 ond) of the gas layer leads to periodic flow disturbances that
 80 control boundary layer separation and reduce acoustic noise
 81 at the Mach number close to one.

82 Subsequently, Unfer and Boeuf¹³ presented a self-
 83 consistent model for nanosecond pulsed actuator. They
 84 showed spatial and temporal distribution of the gas pressure
 85 perturbation induced by the discharge. These results have
 86 been qualitatively compared with Starikovskii *et al.*¹² How-
 87 ever, a detailed study of the physics nanosecond pulsed DBD

^{a)}Present address: Department of Mechanical Engineering, Yuan Ze University, Chung-Li, Taoyuan 32003, Taiwan.

^{b)}E-mail: roy@ufl.edu.

87 actuator is crucial for improving the design and performance
88 of such device.

89 The aim of this work is to simulate and compare the dif-
90 ferences between conventional DBD and nanosecond pulsed
91 DBD to understand the physics of plasma-flow interactions
92 induced by above two different modes. In the experiment of
93 phase-locked particle image velocimetry,¹⁴ they found the
94 negative ions play a dominant role in plasma actuation.
95 Therefore, it is important to implement a three-species
96 plasma model including positive ions, negative ions, and
97 electrons. Simulation details of these charged species using a
98 drift-diffusion form fully coupled with Poisson's equation
99 for electric potential are given in Sec. II. This physical model
100 has been widely used and gives reasonable electro-
101 hydrodynamic (EHD) force distribution to the neutral gas.
102 Section III describes numerical approach of finite element
103 based multiscale ionized gas (MIG) flow code. Section IV
104 presents the computational domain and simulation results for
105 two specific cases simulated, namely, radio frequency (RF)
106 powered and nanosecond pulsed DBD actuators. Conclu-
107 sions are summarized in Sec. V.

108 II. NUMERICAL MODELING

109 A three-species hydrodynamic model^{10,13} is employed
110 for multi-scale plasma discharge simulation at atmospheric
111 pressure. The model uses an efficient finite element algo-
112 rithm. The unsteady transport for positive ions, negative
113 ions, as well as electrons is derived from fluid dynamics in
114 the form of mass and momentum conservation equations.
115 The species momentum is modeled using the drift-diffusion
116 approximation under isothermal condition that can be
117 derived from the hydrodynamic equation. At atmospheric
118 pressure, the drift-diffusion approximation is reasonable and
119 computationally efficient. The continuity equations for pos-
120 itive ions, negative ions, and electrons are given by

$$121 \frac{\partial n_p}{\partial t} + \frac{\partial(n_p V_j)}{\partial x_j} = \alpha |\Gamma_e| - r_{ep} n_p n_e - r_{mp} n_p n_m, \quad (1)$$

$$122 \frac{\partial n_m}{\partial t} + \frac{\partial(n_m V_j)}{\partial x_j} = \eta |\Gamma_e| - r_{mp} n_m n_p, \quad (2)$$

$$123 \frac{\partial n_e}{\partial t} + \frac{\partial(n_e V_j)}{\partial x_j} = (\alpha - \eta) |\Gamma_e| - r_{ep} n_e n_{pe}, \quad (3)$$

$$124 |\Gamma_e| = \sqrt{\sum_j (n_e V_j)^2}, 1 \leq j \leq 2, \quad (4)$$

125 where $n_{p,m,e}$ are the number densities of the charged particle,
126 subscript p , m , and e are positive ions, negative ions, and
127 electrons, respectively. $V_{p,m,e}$ are the species hydrodynamic
128 velocities, α is the ionization coefficient, η is the attachment
129 coefficient, $r_{ep,mp}$ are the electron-ion and ion-ion recombi-
130 nation coefficients, $|\Gamma_e|$ is the electronic flux, and subscript
131 j is the coordinate direction (i.e., $j=x, y$). Here, we neglect
132 the magnetic field effect in the drift-diffusion approximation.
133 The ionic and electronic fluxes in Eqs. (1)–(3) are written as

$$134 n_p V_p = n_p \mu_p \mathbf{E} - D_p \nabla n_p, \quad (5)$$

$$135 n_m V_m = -n_m \mu_m \mathbf{E} - D_m \nabla n_m, \quad (6)$$

$$136 n_e V_e = -n_e \mu_e \mathbf{E} - D_e \nabla n_e, \quad (7)$$

137 where the electrostatic field is given by $\mathbf{E} = -\nabla \phi$, $\mu_{p,m,e}$ are
138 the charged particle mobilities, which are based on tabulated
139 functions of the reduced electric field (E/N),¹⁵ $D_{p,m,e}$ are the
140 diffusion coefficients calculated from the Einstein relation
141 $D_{p,m,e} = \mu_{p,m,e} k_B T_{p,m,e} / e$, which is a function of the mobility
142 ($\mu_{p,m,e}$), Boltzmann's constant (k_B), the constant tempera-
143 tures ($T_{p,m} = 300 \text{ K}$ and $T_e = 11600 \text{ K}$), and the elementary
144 charge ($e = 1.6022 \times 10^{-19} \text{ C}$). The ion and electron drift
145 velocities depend mainly on the electric field. So all the
146 transport coefficients are expressed as a function of a
147 reduced electric field (E/N). The working gas is an air-like
148 N_2/O_2 mixture. The mobilities, diffusion rates, and rate coef-
149 ficients for air-like mixture are obtained from the Refs.
150 15–17. The relation between electric field (\mathbf{E}) and charge
151 separation (q) is given by the Poisson's equation
152

$$153 \nabla \cdot (\epsilon \mathbf{E}) = e(n_p - n_m - n_e) = q, \quad (8)$$

154 where ϵ is the permittivity.

155 The coupled systems of species Eqs. (1)–(3) as well as
156 Poisson's Eq. (8) are solved using the in-house MIG flow
157 code described in Sec. III. The following boundary condi-
158 tions are enforced. At the exposed electrode, the electronic
159 flux is based on the electron thermal velocity and is directed
160 towards the electrode. The positive ion flux normal to the
161 exposed electrode is considered as zero if the electric field is
162 greater than zero. In the plasma domain of top, left, and right
163 boundaries, the homogeneous Neumann boundary condition
164 is imposed (i.e., the slopes of the solution variables are equal
165 to zero). The initial ion and electron number densities are
166 assumed to be uniform and equal to 10^{15} m^{-3} in the plasma
167 domain, while the charged particle densities are equal to
168 zero in the dielectric material.

169 The effect of plasma actuation and the gas heating are
170 incorporated into the compressible Navier-Stokes flow equa-
171 tions through the time-averaged source terms shown below

$$172 \frac{\partial \rho}{\partial t} + \nabla \cdot (\rho \mathbf{V}_n) = 0, \quad (9)$$

$$173 \frac{\partial(\rho \mathbf{V}_n)}{\partial t} + \nabla \cdot (\rho \mathbf{V}_n \mathbf{V}_n) = -\nabla p + \nabla \cdot (\boldsymbol{\tau}) + \mathbf{F}_E, \quad (10)$$

$$174 \frac{\partial(\rho E_n)}{\partial t} + \nabla \cdot [\mathbf{V}_n(\rho E_n + p)] = \nabla \cdot (k \nabla T_n + \boldsymbol{\tau} \cdot \mathbf{V}_n) + \mathbf{P}_{Th}, \quad (11)$$

175 where ρ is the fluid density, \mathbf{V}_n is the neutral gas velocity,
176 p is the pressure, $\boldsymbol{\tau}$ is the stress tensor, E_n is the total specific
177 energy, k is the conductivity, and T_n is the neutral gas tem-
178 perature. For the momentum equations, the electric force
179 density is described as $\mathbf{F}_E = \frac{1}{w} \left[\sum_{j=1}^w e(n_p - n_m - n_e) \mathbf{E} \right]$, and
180 w is the number of time stations in a cycle used for time-
181 averaging. For the energy equations, the power deposition
182 can be assumed as $\mathbf{P}_{Th} = \frac{1}{w} \left[\sum_i^w (\mathbf{J}_p - \mathbf{J}_m) \cdot \mathbf{E} - \xi_{EX} \mathbf{J}_e \cdot \mathbf{E} \right]$,
183 where \mathbf{J} is the current density and ξ_{EX} is the 28% of the
184

201 electron energy deposited into excited states of the gas.¹⁸ A
 202 commercial flow solver, ANSYS FLUENT, is used for flow simu-
 203 lation where EHD force \mathbf{F}_E and gas heating \mathbf{P}_{Th} are incor-
 204 porated as source terms in the momentum and energy equations
 205 via user defined functions (UDFs).

206 III. NUMERICAL APPROACH

207 The plasma modeling approach uses an efficient, parallel,
 208 finite element algorithm¹⁹ anchored in the MIG flow code.
 209 MIG is a modular code and has been developed and verified
 210 with one-, two-, and three-dimensional plasma and fluid-
 211 thermal problems. These problems include slip/transitional
 212 flows through micro/nanoscale geometries, modeling of the
 213 Hall effect thrusters using multispecies and two-temperature
 214 physics. Specifically, MIG has been used to model dielectric
 215 barrier discharges for subsonic flow control at atmospheric
 216 conditions.^{3,4,7-9} The finite element based modeling allows
 217 boundary conditions to be easily implemented.

218 Systems of nonlinear partial differential equations can be
 219 solved using the finite element based MIG code. If we denote
 220 the differential equation using an operator $L(\cdot)$, then the sys-
 221 tem of equations can be written as $L(\theta) = 0$ where θ is the
 222 unknown state variables. Multiplying this equation by a per-
 223 missible test function ψ and integrating over a discretized do-
 224 main Ω yields the Galerkin weak statement (GWS). The test
 225 function in the GWS is chosen orthogonal to the trial function
 226 to ensure the minimum error. The resulting matrix equation is
 227 solved with the nonlinear Newton-Raphson scheme using a
 228 generalized minimal residual (GMRES) solver to handle the
 229 sparseness of the stiffness matrix. The system utilizes a sub-
 230 grid embedded (SGM) algorithm²⁰ for computational stability
 231 and control of dispersion error. The SGM algorithm is incor-
 232 porated into the dissipative flux terms based on the local
 233 cell velocity and is expected to ensure a nodewise mono-
 234 tone solution. For plasma application in 2-D, a nodewise mono-
 235 tone distribution (subscript i) SGM parameter is $r_i = \frac{|V_i| h_i}{\gamma_i D_i}$, where

236 the $\gamma_i = \sqrt{\frac{1-A_e}{D_i h_i}}$ is a correlation function, V_i is the drift velocity,
 237 h_i is the element size, D_i is the diffusion parameter, and
 238 A_e is the area of the element. The convergence criterion is
 239 based on the L_2 norms of the change in the solution $\Delta\theta$ and
 240 the residual at each time step. The convergence criterion for
 241 the problem is met when the residuals for all state variables
 242 fall below a chosen number of 10^{-4} .

243 In the present work, we assume that the plasma effects
 244 can be loosely coupled to the compressible Navier-Stokes
 245 equations through the body force and energy source terms,
 246 which depend on the net space charge, ionic, and electronic
 247 fluxes as well as electric field distributions. Due to large time
 248 scales difference between electrons (nanosecond), ions (i.e.,
 249 microsecond), and fluid flow (i.e., millisecond), we neglect
 250 the flow effect on the plasma formation.

251 IV. RESULTS AND DISCUSSION

252 A. Computational domain

253 Figures 1(a) and 1(b) show the computational dimen-
 254 sions of $1 \times 0.5 \text{ cm}^2$ for the plasma domain and $3 \times 1 \text{ cm}^2$

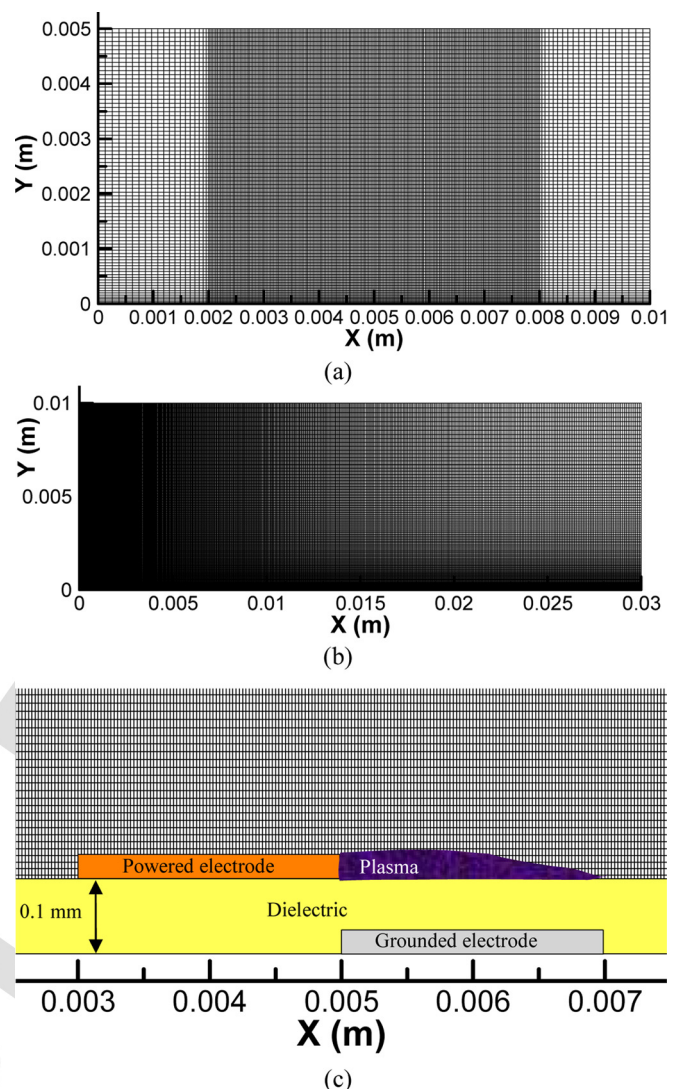


FIG. 1. The computational grids of (a) plasma domain and (b) fluid flow domain. (c) Zoom of the dielectric barrier discharge actuator near the plasma region.

255 for the fluid flow domain, respectively. These grids corre-
 256 spond the sizes of 90 321 and 60 701 nodes, respectively.
 257 The smallest cell size is $25 \mu\text{m}$ for both domains suitable to
 258 resolve the sheath structure. Figure 1(c) shows a zoomed in
 259 view of the DBD actuator. The DBD actuator consists of two
 260 electrodes separated by a 0.1 mm thick dielectric layer of rel-
 261 ative constant $\epsilon = 5\epsilon_0$ (where $\epsilon_0 = 8.854 \times 10^{-12} \text{ F/m}$ is the
 262 permittivity in vacuum). Both exposed power and buried
 263 ground electrodes are 2 mm long. The thickness of the elec-
 264 trodes is assumed to be negligible. Also, the gap between
 265 electrodes in horizontal direction is assumed to be zero.
 266

267 In order to understand the physics of plasma force mech-
 268 anism for flow control, we present two cases of RF powered
 269 and nanosecond pulsed DBD actuators. Figure 2 shows the
 270 calculated total linear current density and applied voltage for
 271 these two different modes. For the case of RF powered DBD
 272 actuator, the exposed electrode is driven by sinusoidal wave-
 273 form with amplitude of 0.5 kV and frequency of 1000 kHz.
 274 We can consider a period of time from $4.5 \mu\text{s}$ to $5.5 \mu\text{s}$ for
 275 the sine wave shown in Figure 2. There are two slopes,
 276 which are the positive-going (when the slope of the applied
 277

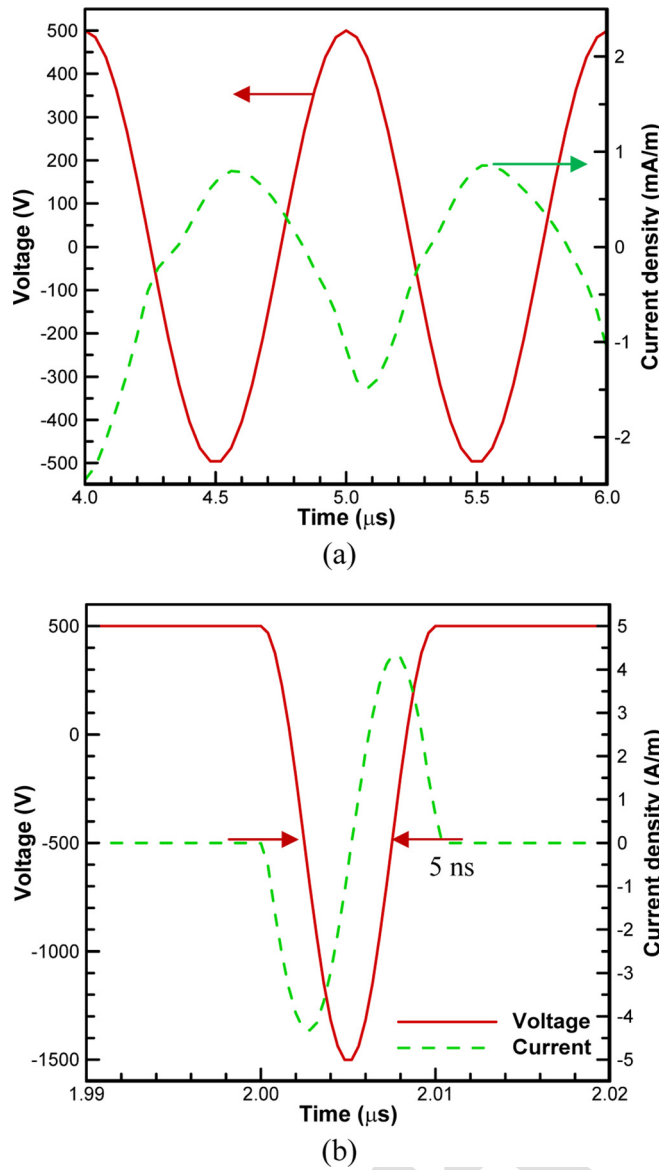


FIG. 2. Calculated total linear current density (dashed line) and applied voltage (solid line) for (a) amplitude of 0.5 kV and frequency of 1000 kHz sinusoidal waveform and (b) nanosecond pulse of -2 kV amplitude with repetition rate of 500 kHz superimposed on a dc bias of 0.5 kV; FWHM of 5 ns.

voltage is positive) and the negative-going (opposite direction of the positive-going) discharges. We can see an uneven peak linear current density passing through the exposed electrode for both slopes. The peak linear current density estimates around 1 mA/m for the positive-going discharge and 1.5 mA/m for the negative-going discharge. The uneven peak linear current density may explain why the forward EHD force (i.e., momentum transfer) dominates the flow field. For the case of nanosecond pulsed DBD actuator, the exposed electrode is driven by negative pulses of -2 kV amplitude and repetition rates of 500 kHz superimposed on a positive dc bias shown in Figure 2(b). The full width at half maximum (FWHM) of the pulse is 5 ns. The calculated total linear current density of the nanosecond pulsed actuator is much higher than the RF powered actuator. This instantaneous surge may be the reason why the gas heating (i.e., energy

transfer) becomes the main mechanism of impact for the nanosecond pulsed DBD actuator.

B. Plasma dynamics for RF powered DBD actuator

In order to understand the physics of RF powered DBD actuator, we can consider two separate slopes of sine wave. Figure 3 shows the electric potential, net charges, force, and power density distribution at 4.56 μ s (i.e., positive-going discharge). At this instant, the electric potential varies from -465 to 0 V shown in Figure 3(a). During the negative half-cycle of the discharge, the exposed electrode (colored by orange) plays the role of the cathode (i.e., emits electrons if electric field is high enough). Some electrons may escape from molecules or atoms due to ionization process. Some electrons may attach to oxygen and form negative ions. The net charge separation is based on the temporal and spatial distribution of these positive ions, negative ions, and electrons shown in Figure 3(b). Figure 3(c) shows the horizontal force magnitude overlaid on force vectors. While the positive ions are attracted to the cathode (i.e., exposed electrode), the part of the horizontal force vectors is acting to the left based on the direction of the electric field. At this instant, the peak of the power deposition is around six orders of magnitude shown in Figure 3(d). For the negative-going discharge shown in Figure 4, we can see the same style of contours for electric potential, net charge separation, horizontal force magnitude overlaid on force vectors, and power deposition at 5.08 μ s. The peak applied voltage is equal to 438 V at the exposed electrode shown in Figure 4(a). During this positive half-cycle of the discharge, the negative ions and electrons are attracted by the anode (i.e., the exposed electrode), while the positive ions move towards the dielectric surface. The strongest net charge is close to the tip of exposed electrode due to very high electric field ($\sim 3 \times 10^6$ V/m). Compared with Figure 3(c), the horizontal force magnitude in Figure 4(c) is much stronger and imparts momentum forward downstream to the neutral gas. For the power deposition, both cycles have very similar energy distribution near the tip of the exposed electrode.

C. Plasma dynamics for nanosecond pulsed DBD actuator

Literature^{10,11} shows the combination of dc bias and repetitive nanosecond pulses may efficiently generate the plasma. The reason may be most of discharges happen in the negative-going of a sinusoidal signal.²¹ In such powering scheme, the nanosecond pulsed signals generate multiple negative-going discharges and produce stronger effect on the flow than a conventional sine wave. Figures 5 and 6 show the contours of applied voltage, net charge separation, horizontal force overlaid on force vectors, and power deposition at the peak pulse voltage (i.e., potential equals -1.5 kV) and after the pulse (i.e., potential equals 0.5 kV), respectively. Figure 5(a) shows the electric potential varies from -1.5 kV to 0 V corresponding to the signal at 2.0048 μ s. We can see high concentration of positive ions and negative ions happen near the tip of the exposed electrode due to strong electric field shown in Figure 5(b). During the negative pulse, we can

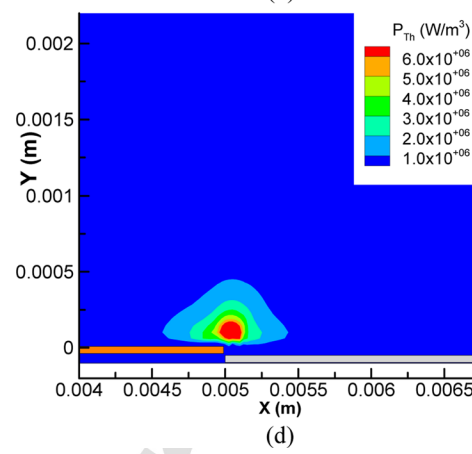
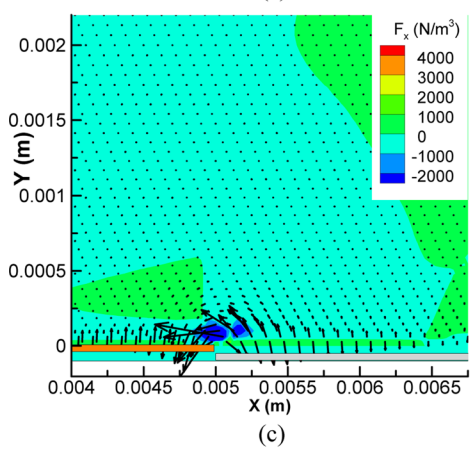
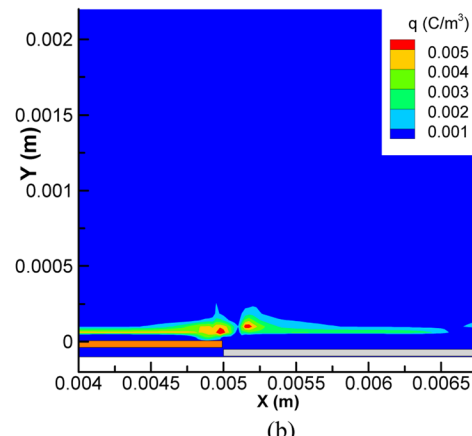
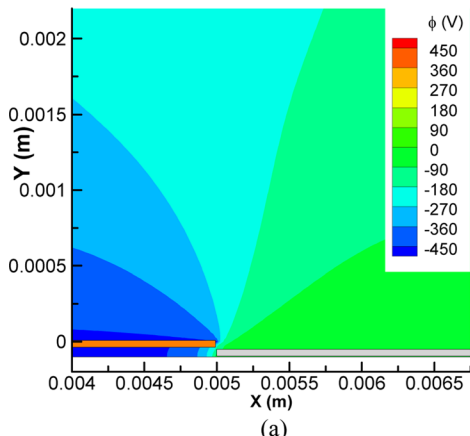


FIG. 3. Contours of (a) electric potential (V), (b) charged separation (C/m^3), (c) horizontal force magnitude (N/m^3) with force vectors, and (d) power deposition (W/m^3) for DBD actuator driven by sinusoidal waveform at $4.56 \mu s$.

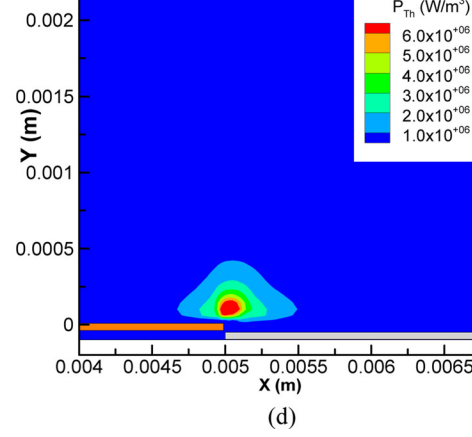
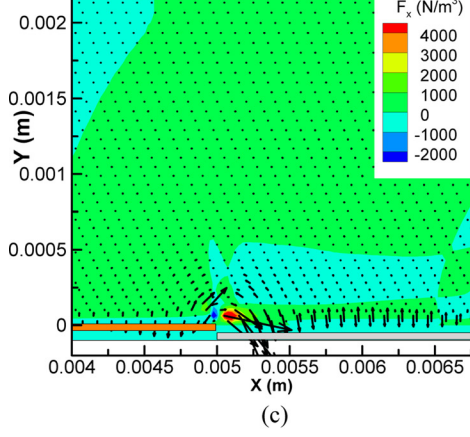
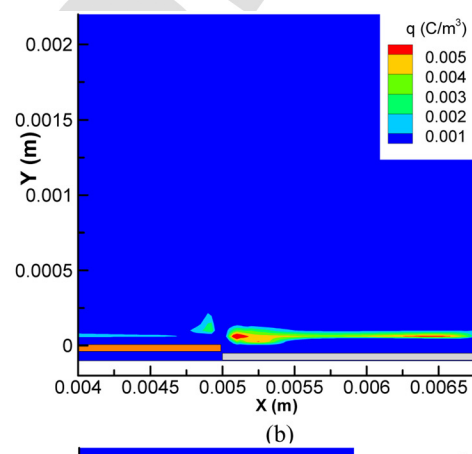
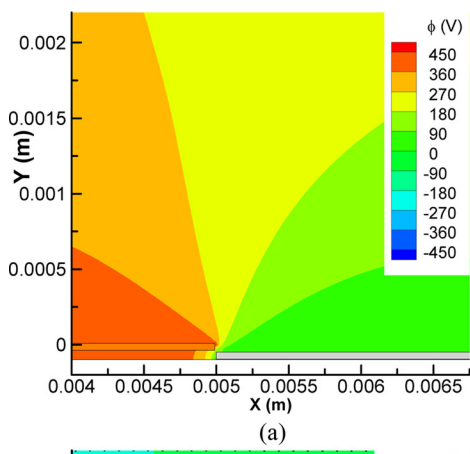


FIG. 4. Contours of (a) electric potential (V), (b) charged separation (C/m^3), (c) horizontal force magnitude (N/m^3) with force vectors, and (d) power deposition (W/m^3) for DBD actuator driven by sinusoidal waveform at $5.08 \mu s$.

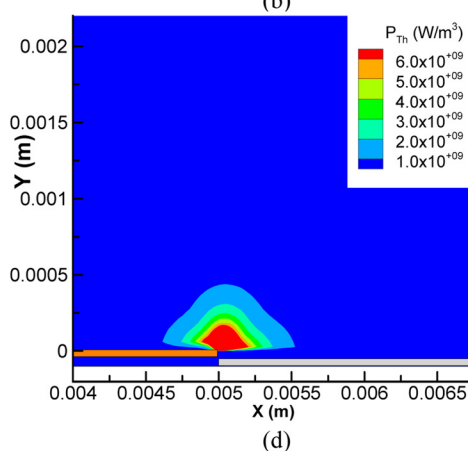
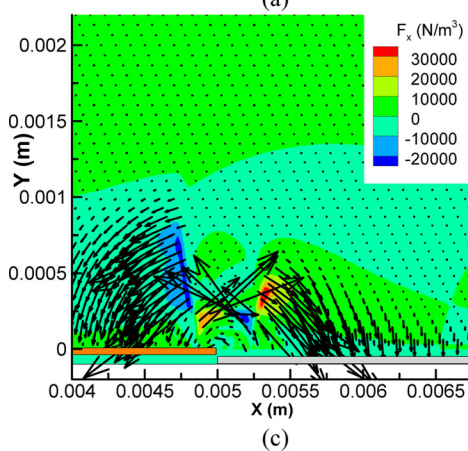
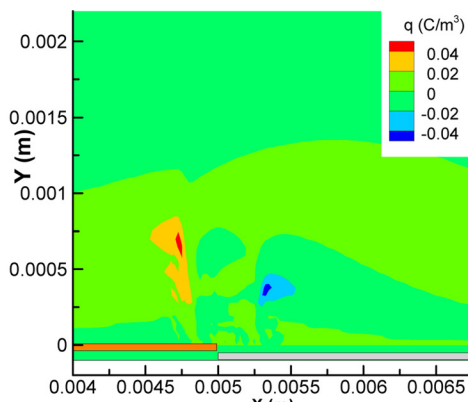
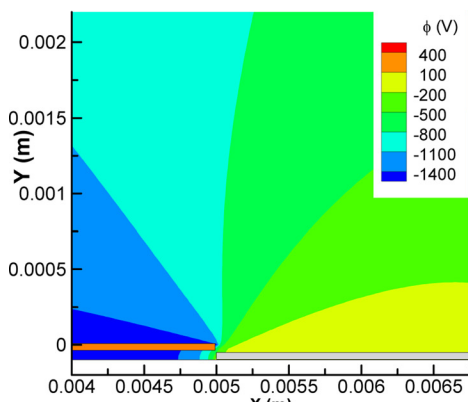


FIG. 5. Contours of (a) electric potential (V), (b) charged separation (C/m^3), (c) horizontal force magnitude (N/m^3) with force vectors, and (d) power deposition (W/m^3) for nanosecond pulsed DBD actuator driven at $2.0048 \mu s$.

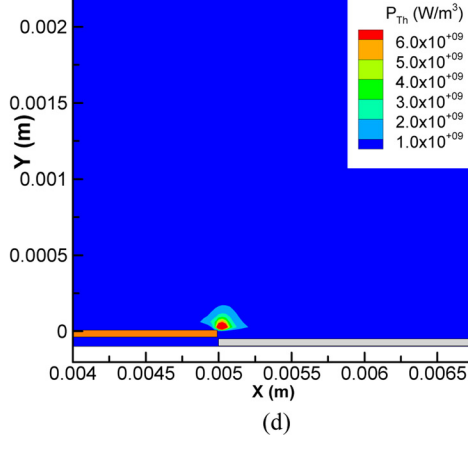
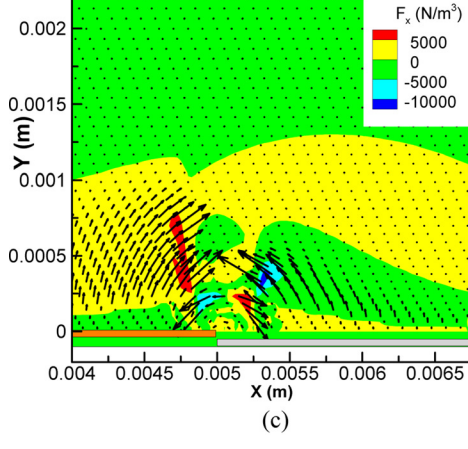
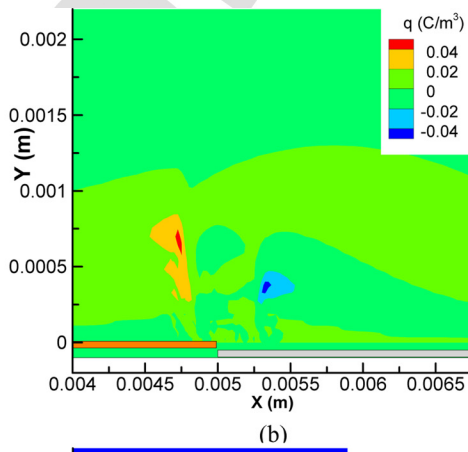
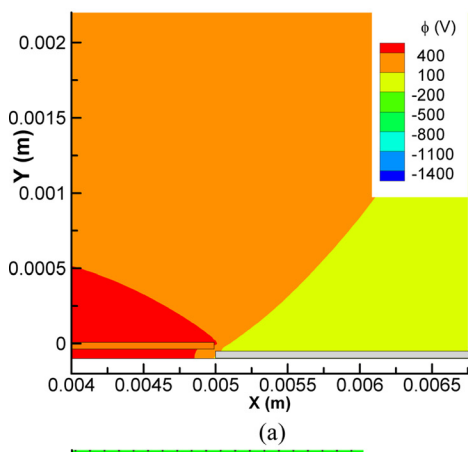


FIG. 6. Contours of (a) electric potential (V), (b) charged separation (C/m^3), (c) horizontal force magnitude (N/m^3) with force vectors, and (d) power deposition (W/m^3) for nanosecond pulsed DBD actuator driven at $2.01 \mu s$.

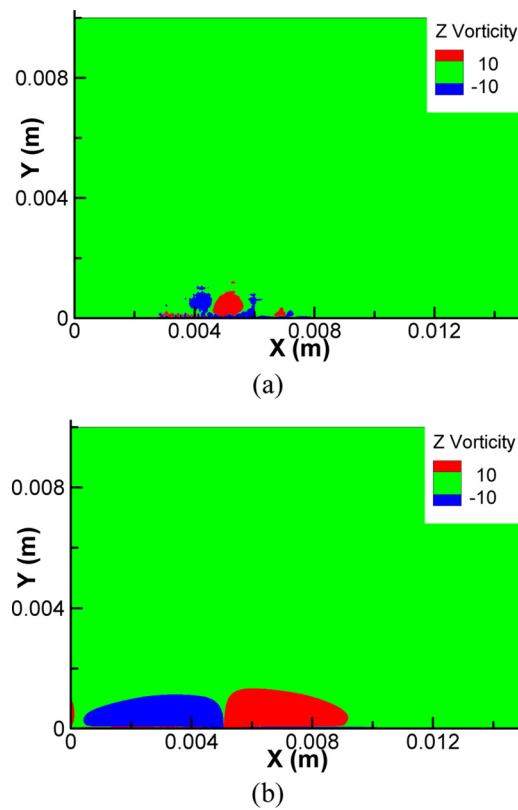


FIG. 7. Contours of z-vorticity induced by (a) RF powered DBD actuator at 10 ms and (b) nanosecond pulsed DBD actuator at 10 μ s.

348 clearly see both upstream-directed force and downstream-
 349 directed force on the same orders of magnitude shown in
 350 Figure 5(c). After time integration of the negative pulse, the
 351 time average of horizontal force becomes small (i.e., tens of
 352 N/m^3). Such small amount EHD force may not have signifi-
 353 cant contribution to momentum transfer. The peak deposited

power in W/m^3 , shown in Figures 6(d), is of the order of ten 354
 that is four orders of magnitude higher than conventional 355
 DBD actuator. This may be a reason why the main mecha- 356
 nism of impact is dominated by energy transfer for the nano- 357
 second pulsed DBD actuator. 358

D. Gas dynamics induced by RF powered and 359 nanosecond pulsed DBD actuator 360

To see the effects of DBD actuator driven by two differ- 361
 ent modes, we employ time-averaged EHD force density and 362
 power deposition on a quiescent flow domain. Figure 7(a) 363
 shows unsteady airflow induced z-vortices by RF powered 364
 DBD actuator, while Figure 7(b) plots the airflow generated 365
 z-vortices by nanosecond pulsed DBD actuator. For both 366
 cases, the induced velocity is quite small (~ 0.1 – 0.2 m/s) at 367
 this low-voltage of sinusoidal signal and nanosecond pulses. 368
 The local body force generated by the RF signal entrains 369
 fluid from the upstream to the downstream of the actuator. 370
 The vorticity contour near the wall ($y = 5$ mm) distinct 371
 clockwise and counter-clockwise vortex pair due to entrain- 372
 ment and plasma induced jet. The flow response is in milli- 373
 seconds. For the case of nanosecond pulsed actuator shown 374
 in Figure 7(b), the flow response seems quite different. The 375
 flow response is very fast within a few microseconds because 376
 the flow physics is mainly dominated by energy transfer. The 377
 vortices induced by nanosecond pulsed actuator propagate 378
 much faster than RF powered actuator. The maximum 379
 induced streamwise velocity generated by nanosecond pulses 380
 equals 0.23 m/s. This value is on the same order of magni- 381
 tude with the experimental data from Starikovskii¹² demon- 382
 strating that nanosecond pulsed DBD actuator does not 383
 induce significant flow velocity. 384

Figures 8(a)–8(c) show the dynamics of the computed 385
 shock wave structure emanating from the nanosecond pulsed 386

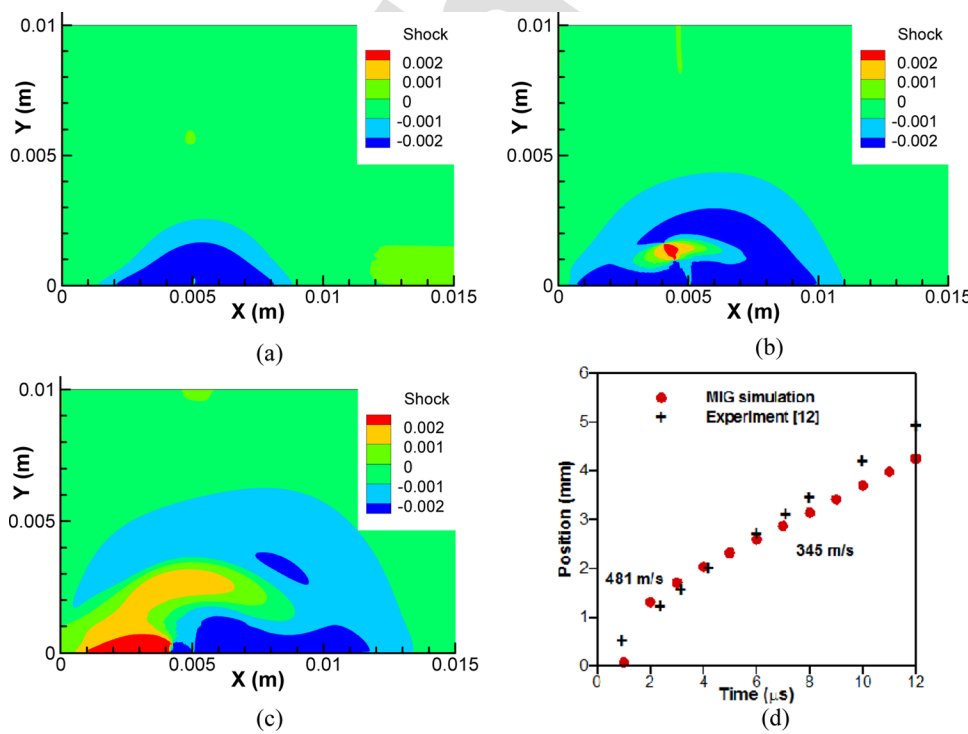


FIG. 8. Contours of shock wave induced by nanosecond pulsed DBD actuator at (a) 8 μ s, (b) 16 μ s, and (c) 25 μ s. (d) Calculated pressure wave propagation speed from the surface at location of $x = 5.1$ mm and pressure of 12 Pa compared with experimental data from Starikovskii.¹²

387 DBD actuator at 8, 16, and 25 μ s. The shock is defined as
 388 function of $\mathbf{V}_n \cdot \nabla p / (a|\nabla p|)$, where a is the speed of sound.
 389 These results show that the semicircular domain within
 390 which the pressure variation is increasing with time due to
 391 large energy deposition at the tip of the exposed electrode.
 392 These results qualitatively compare well with experimental
 393 shadow images from Starikovskii *et al.*¹² Also, the propagation
 394 velocity of the pressure (p) wave is calculated and plotted
 395 in Figure 8(d). During the first two microseconds, we can
 396 see the propagation speed is much faster (~ 480 m/s) and
 397 then quickly decreased to about 280 m/s. The same phenomenon
 398 is also observed from experimental data¹² although in
 399 that case a sonic speed was estimated for the first twelve
 400 microseconds.

401 V. CONCLUSIONS

402 We have studied a self-consistent plasma model for RF
 403 powered and nanosecond pulsed DBD actuators in air. Three
 404 species of positive ions, negative ions, and electrons have
 405 taken into account. In order to obtain temporal and spatial dis-
 406 tribution of charged species, the coupled system of continuity
 407 equations and Poisson's equation are solved based on finite
 408 element based MIG flow code. Fluid flow domain is also
 409 solved in a loosely coupled manner using time averaged EHD
 410 force and power deposition source terms in compressible
 411 Navier-Stokes equations. At the beginning of the negative-
 412 going part of the cycle at 4.56 μ s, the motion of negative ions
 413 and electrons generate an EHD force directed toward the
 414 grounded electrode. Such time averaged EHD force creates a
 415 near wall jet through momentum transfer to the neutral gas.
 416 For the case of nanosecond pulsed DBD actuator, the time
 417 averaged EHD force is quite small while the scalar thermal
 418 energy deposition near the tip of the exposed electrode is
 419 large. The gas dynamics induced by energy deposition shows
 420 nanosecond pulsed actuator is able to create acoustic pressure
 421 waves within a few microseconds. Such acoustic jets may
 422 affect the onset of boundary layer separation.

423 In summary, we compared the charge distribution
 424 between sinusoidal DBD and nanosecond pulsed DBD that
 425 showed a fundamentally different mechanism in momentum
 426 transfer. We also compared the power deposition mechanism
 427 between sinusoidal DBD, and nanosecond pulsed DBD that
 428 showed a fundamentally different mechanism in energy trans-
 429 fer. Based these results, we then calculated the average force
 430 and power and apply them to find induced vorticity distribu-
 431 tion for both cases. The results show that the flow response
 432 for nanosecond DBD is much faster and is in microseconds.
 433 To our knowledge, this has not been reported elsewhere. We
 434 validated our numerical results for nanosecond pulsed DBD

with available experimental data and found a good agree-
 435 ment. Important applications are foreseeable for fixed and
 436 moving airfoils in airplanes, helicopters, and wind turbines.
 437

438
 1 T. C. Corke and C. L. Enloe, "Dielectric barrier discharge plasma actuators for flow control," *Rev. Fluid Mech.* **42**, 505 (2010).
 439
 2 N. Mastanaiah, C.-C. Wang, J. Johnson, and S. Roy, "A computational
 440 diagnostic tool for understanding plasma sterilization," in *49th AIAA Aerospace Sciences Meeting and Exhibit*, AIAA Paper 2011-908, 2011.
 441
 3 C.-C. Wang, R. J. Durscher, and S. Roy, "Three-dimensional effects of
 442 curved plasma actuators in quiescent air," *J. Appl. Phys.* **109**, 083305 (2011).
 443
 4 C.-C. Wang and S. Roy, "Combustion stabilization using serpentine
 444 plasma actuators," *Appl. Phys. Lett.* **99**, 041502 (2011).
 445
 5 S. O. Macheret, M. N. Shneider, and R. B. Miles, "Modeling of air plasma
 446 generation by repetitive high-voltage nanosecond pulses," *IEEE Trans. Plasma Sci.* **30**, 1301 (2002).
 447
 6 R. J. Durscher and S. Roy, "Force measurement techniques and preliminary
 448 results using aerogels and ferroelectrics for dielectric barrier discharge actuators," in *41st AIAA Fluid Dynamics Conference and Exhibit*,
 449 AIAA Paper 2011-3735, 2011.
 450
 7 C.-C. Wang and S. Roy, "Flow shaping using three-dimensional micro-
 451 scale gas discharge," *Appl. Phys. Lett.* **95**, 081501 (2009).
 452
 8 C.-C. Wang and S. Roy, "Three-dimensional simulation of a micro plasma
 453 pump actuator," *J. Phys. D: Appl. Phys.* **42**, 185206 (2009).
 454
 9 C.-C. Wang and S. Roy, "Microscale plasma actuators for improved thrust
 455 density," *J. Appl. Phys.* **106**, 013310 (2009).
 456
 10 A. V. Likhanskii, M. N. Shneider, S. O. Macheret, and R. B. Miles,
 457 "Modeling of dielectric barrier discharge plasma actuator in air," *J. Appl. Phys.* **103**, 053305 (2008).
 458
 11 D. F. Opaits, A. V. Likhanskii, G. Neretti, S. Zaidi, M. N. Shneider, S. O.
 459 Macheret, and R. B. Miles, "Experimental investigation of dielectric bar-
 460 rier discharge plasma actuators driven by repetitive high-voltage nanosec-
 461 ond pulses with dc or low frequency sinusoidal bias," *J. Appl. Phys.* **104**,
 462 043304 (2008).
 463
 12 A. Y. Starikovskii, A. A. Nikipelov, M. M. Nudnova, and D. V. Roupas-
 464 sov, "SDBD plasma actuator with nanosecond pulse-periodic discharge,"
 465 *Plasma Sources Sci. Technol.* **18**, 034015 (2009).
 466
 13 T. Unfer and J. P. Boeuf, "Modeling of a nanosecond surface discharge
 467 actuator," *J. Phys. D: Appl. Phys.* **42**, 194017 (2009).
 468
 14 W. Kim, H. Do, M. G. Mungal, and M. A. Cappelli, "On the role of oxy-
 469 gen in dielectric barrier discharge actuation of aerodynamic flows," *Appl. Phys. Lett.* **91**, 181501 (2007).
 470
 15 G. J. M. Hagelaar and L. C. Pitchford, "Solving the Boltzmann equation to
 471 obtain electron transport coefficients and rate coefficients for fluid mod-
 472 els," *Plasma Sources Sci. Technol.* **14**, 722–733 (2005).
 473
 16 H. W. Ellis, R. Y. Pai, E. W. McDaniel, E. A. Mason, and L. A. Viehland,
 474 "Transport properties of gaseous ions over a wide energy range," *At. Data Nucl. Data Tables* **17**, 177–210 (1976).
 475
 17 I. A. Kossyi, A. Y. Kostinsky, A. A. Matveyev, and V. P. Silakov, "Kinetic
 476 scheme of the non-equilibrium discharge in nitrogen-oxygen mixtures,"
 477 *Plasma Sources Sci. Technol.* **1**, 207–220 (1992).
 478
 18 A. Flitti and S. Pancheshnyi, "Gas heating in fast pulsed discharges in
 479 N_2O_2 mixtures," *Eur. Phys. J. Appl. Phys.* **45**, 21001 (2009).
 480
 19 A. J. Baker and D. W. Pepper, *Finite Element 1-2-3* (McGraw Hill, 1991).
 481
 20 S. Roy and A. J. Baker, "Nonlinear, subgrid embedded finite-element basis
 482 for accurate, monotone, steady CFD solutions," *Numer. Heat Transfer, Part B* **31**, 135–176 (1997).
 483
 21 C. L. Enloe, M. G. McHarg, and T. E. McLaughlin, "Time-correlated force
 484 production measurements of the dielectric barrier discharge plasma aero-
 485 dynamic actuator," *J. Appl. Phys.* **103**, 073302 (2008).
 486